LA-UR-08-0012

Approved for public release;
distribution is unlimited.

Title:	Microstructure, texture, and residual stress in a friction stir processed AZ31B magnesium alloy
Author(s):	W. Woo, H. Choo, M. B. Prime, Z. Feng, and B. Clausen
Details:	Acta Materialia, 56(8), 1701-1711, 2008.

Microstructure, texture, and residual stress in a friction stir processed AZ31B magnesium alloy

W. Woo [a, b], H. Choo [a, b*], M. B. Prime [c], Z. Feng [b], and B. Clausen [d]

[a] *Department of Materials Science and Engineering, The University of Tennessee, Knoxville, TN 37996, USA*

[b] *Materials Science and Technology Division, Oak Ridge National Laboratory, Oak Ridge, TN 37831, USA*

[c] *Analysis and Prediction Group, Los Alamos National Laboratory, Los Alamos, NM 87545, USA*

[d] *Los Alamos Neutron Science Center, Los Alamos National Laboratory, Los Alamos, NM 87545, USA*

***Corresponding Author:**

Hahn Choo

The University of Tennessee

Department of Materials Science and Engineering

319 Dougherty Engineering Building

Knoxville, TN 37996-2200

Tel 865 974 3643

Fax 865 974 4115

Email: hchoo@utk.edu

(Manuscript to be submitted to: *Acta Materialia*)

*Author to whom correspondence should be addressed; electronic mail: hchoo@utk.edu

Abstract

Spatial variations of microstructure, hardness, chemical composition, tensile behavior, texture, and residual stresses were investigated in a friction-stir processed (FSP) AZ31B magnesium alloy. The residual stresses were measured using two different methods: neutron diffraction and contour method. No significant variations in the hardness and chemical compositions are found in the FSP zones including the severely-deformed stir zone (SZ), which shows a finer grain size compared to the heat-affected zone and base material. On the other hand, significant changes in the tensile yield strength, texture, and residual stresses are observed in the FSP zones. The relationship between the texture variations and yield-strength reduction; and its influence on the decrease in the residual stress near the SZ is discussed. Finally, the residual stresses measured by neutron diffraction and contour method are compared, and the effect of the texture on the neutron-diffraction residual stress measurements is discussed.

Keywords: Magnesium alloys, Friction stir welding, Microstructure, Residual stress, Neutron diffraction, Contour method, Texture

1. Introduction

Friction-stir welding (FSW) is a newly developed joining process that attracts tremendous interest in research and applications due to numerous advantages over traditional fusion welding, including nearly defect-free welds with minimized cracking, fine grain structures, and minimized distortion [1]. FSW uses a rotating tool consisting of a threaded pin and shoulder to apply severe plastic deformation and frictional heating to the base metal and produce a strong metallurgical joint, which is achieved in solid state during welding [2]. Friction-stir processing (FSP), a variation of FSW, is used to modify the material microstructure and the examples include localized grain refinements and homogenization of precipitate particles [3]. The economical and technological benefits of FSW/FSP have been well recognized in various engineering materials [4].

Magnesium alloys have been receiving significant attention in the transportation industry as lightweight structural materials for energy efficient vehicles. Various studies have recently been reported on the FSW/FSP of Mg alloys and the topics can be classified into three categories: (i) microstructure and hardness [5-12], (ii) texture and fracture [13-15], and (iii) surface modification in metals and composites [16-20].

First, Esparza *et al.* investigated the characteristic grain structure such as recrystallized stir zone (SZ), transition zone (TZ), and base material (BM) in FSW AZ31B Mg alloy and noted no loss of weld-related strength (based on microhardness) in the SZ [5]. Later, Chang *et al*. [6] and Wang *et al*. [7] reported that the smaller grain size in the SZ did not significantly increase the hardness and suggested a weak grain-size dependence in terms of the Hall-Petch relationship in AZ31B Mg alloy. On the other hand, several reports presented significant hardness decreases in the SZ in the case of initially strain-hardened AZ31B-H24 alloy [9-12]. Second, Park *et al.*

observed a strong texture development in FSW AZ61 Mg alloy and suggested that the basal plane is roughly aligned with the surface of the tool pin column in the SZ [13,14]. Woo *et al.* provided the quantitative texture changes using neutron diffraction in FSP AZ31B Mg alloy, which was, in turn, correlated to the reduced yield strength and increased elongation along the longitudinal direction in the SZ [15]. The results showed that the integrity and performance of FSW products can be significantly influenced by the texture changes especially for the Mg alloy, which has the hexagonal close packed (hcp) lattice structure and shows poor workability due to the limited number of available slip systems [21]. Finally, application of the grain-refining capability of FSP to Mg alloys was demonstrated on the highly-formable AZ91D Mg alloy [16], Mg-based composites with SiO_2 or SiC reinforced particles [17,18], and AM60B or AZ91 Mg cast alloys [19,20].

The frictional heating and severe plastic deformation involved in the FSW/FSP can induce significant reisudal stresses. The residual stresses in FSW aluminum alloys have been studied extensively [e.g., 22-28]. Generally, the maximum tensile residual stresses along the welding direction are measured as about 20% ~ 50% of the yield strength of the BM for Al alloys. Furthermore, a recent report showed that the longitudinal residual stress can approach 100% of the yield strength (~300 MPa) of the BM in the FSW 304L stainless steel [29]. However, direct experimental investigation of the residual stress in FSW Mg alloys has not been reported.

In this paper, we present the results of: (1) microstructure, hardness, chemical composition, and tensile behavior of the FSP AZ31B Mg alloy, (2) spatially-resolved measurements of the texture variations and residual stresses using neutron diffraction, and (3) mapping of the residual stresses using contour method. The spatial variations of the residual stresses, which were measured by the two inherently different techniques, will be compared. Most importantly, we

discuss the relationship between the significant texture variations and yield-strength reduction; and its influence on the residual stress profile in the FSP Mg alloy.

2. Processing, Microstructure, and Mechanical Properties

As-received commercial AZ31B Mg alloy plates were used in the hot-rolled and soft-annealed condition (O tempering). The nominal chemical composition in weight percent is 3.0 Al, 1.0 Zn, 0.2 Mn, and balance Mg. The dimension of the FSP specimen was 306 × 306 × 6.5 mm^3, Fig. 1(a). The transverse sides of the plates were clamped to constrain the displacement of the specimen during FSP and the clamping was removed after FSP when the plate was air cooled to 25 °C. The sample was prepared by the "bead-on-plate" method using a single plate instead of joining two pieces of plates.

In order to study the thermal and mechanical effects responsible for the development of the microstructure and stresses during FSP, two FSP cases were examined [25]. A regular FSP plate (*Case 1*) was processed using both the stirring pin and tool shoulder made of an H-13 tool steel and, hence, was subjected to both heating and deformation during FSP. The plate was processed using the following parameters: 0.97 mm/sec traveling speed, 600 rpm clockwise rotating speed, and 8,000 N compressive force using a tool with a 19.05-mm shoulder diameter and a 6.35-mm pin diameter with a 5.72-mm pin height. The tool was tilted 3 degrees opposite to the processing direction, which coincided with the rolling direction of the BM. Note that the advancing side, where the processing and tool rotating directions are the same, is presented as the negative *y* direction (the retreating side is positive) throughout the paper. The LD, TD, and ND denote longitudinal (x), transverse (y), and normal (z) directions of the plate, Fig. 1(a). To minimize the severe plastic deformation and, therefore, isolate thermal effects, a modified FSP plate (*Case 2*)

was processed under the same conditions as *Case 1*, but utilizing a special tool without the stirring pin, Fig. 1(b).

Microstructural characterization was performed at the cross-section (y-z plane) of the FSP plates, Fig. 1(a). The samples were cold-mounted, ground, polished, and etched by a mixture of 4.2 g picric acid, 10 ml acetic acid, 70 ml ethanol, and 10 ml diluted water solution for about 10 s at room temperature for the optical microscopy. Vickers microhardness (H_v) was measured in the "middle" of the plate thickness across the centerline with 1~2 mm horizontal spacing on the polished cross-section using 50 gf applied load, Fig. 1(c). Chemical composition analysis was performed along the same line using energy dispersive spectrometer (EDS). The EDS has a focused electron beam size of 100 × 100 μm with ±3 % of error range for the measured composition. The Mg and Al chemical compositions (wt %) were measured three times at the same position and averaged.

A total of five tensile specimens were machined at positions of 0 mm, ± 10 mm, and ± 20 mm from the centerline with the gage length parallel to the centerline (i.e., longitudinal direction) from both *Cases 1* and *2* plates. The dimensions are 6-mm wide, 6.5-mm thick, and 25-mm long in the gage section following the ASTM E 8M-04. In addition, 20 subsize LD tensile samples were prepared from the *Case 1* plate with dimensions of 4-mm width (along ND), 1.65-mm thickness (along TD) and 25-mm gage length (along LD). The subsize samples were cut every 2 mm across the centerline to probe the spatial variation of the longitudinal tensile yield strength in each characteristic region of the FSP plate. All specimens were prepared using electrical-discharge machining (EDM) and tensile tests were performed using Material Test System (MTS) load frame with hydraulic wedge-grips at a constant crosshead velocity providing an initial strain rate of 6.7×10^{-4} s^{-1} at room temperature.

3. Neutron Diffraction

3.1. Texture measurement

Neutron diffraction is a well-established technique for spatially-resolved measurements of the texture and residual stress inside the bulk materials [30,31]. The SMARTS instrument (Spectrometer for MAterials Research at Temperature and Stress) at LANSCE (Los Alamos Neutron Science CEnter) was used for the measurements of the texture and residual stress [32]. A line scan was performed at the middle of the plate thickness for both *Cases 1* and *2*, Fig. 1(c). First, diffraction along the LD and ND were measured simultaneously using a 2(x) × 2(y) × 2(z) mm^3 scattering volume. Note that 2-mm height (x) and width (z) of incident beam slits and 2-mm radial collimators (y) define the scattering gauge volume. Second, the TD and ND diffractions were measured using a scattering volume of 20(x) × 2(y) × 2(z) mm^3. The intensities of multiple diffractions peaks were analyzed using the single peak fitting (SPF) method in GSAS (General Structure Analysis System) [33] and prismatic $\left(10\bar{1}0\right)$, basal $\left(0002\right)$, and pyramidal $\left(10\bar{1}1\right)$ plane results are presented here.

The integrated intensities (I_τ) of the diffraction peaks provide quantitative insights to the texture variations [30,34]. Specifically, the reduced intensity, which is I_τ divided by λ^4 (wavelength), Z_τ (multiplicity), and $F(\tau)^2$ (structure factor) that vary for each reflection, is proportional to the number of unit cells (N_s) oriented to satisfy Bragg's law within the scattering volume (V_{cell}).

$$I_\tau \propto \left(\frac{\lambda^4 Z_\tau F(\tau)^2}{\sin^2\theta}\right)\left(\frac{N_s}{V_{cell}}\right) \tag{1}$$

Thus, the reduced intensity of a specific (*hkil*) reflection is proportional to the number of unit cells in the scattering volume with their (*hkil*)-plane normal parallel to the scattering vector. More details can be found in refs. 34 and 35.

3.2. Residual stress measurement

Two measurement methods were used to assess residual stresses in FSP Mg alloy, namely neutron diffraction method and contour method. For the residual stress analysis from the neutron diffraction results, the peak-position changes were analyzed from the same data set described in Section 3.1. Note that the LD, TD, and ND were assumed as the three principal directions of the strain tensor in the given plate and the normal component measured twice with reasonable reproducibility observed. For the peak analysis, the SPF and Rietveld peak fitting methods were used [33,36]. While the SPF refines each (*hkil*) reflection, the Rietveld refinement analyzes the entire diffraction profile by comparing the measured profile and calculated one based on the crystallographic space group. The lattice spacings $\left(d_{hkil}\right)$ for each (*hkil*) lattice plane were obtained using the SPF and the lattice parameters for the a-axis $\left(a_a\right)$ and c-axis $\left(a_c\right)$ in hcp structure were analyzed using the Rietveld method.

The residual stress was calculated using a well-established methodology described in elsewhere [e.g., 22-31,37-39]. Briefly, the residual strain from the SPF can be calculated using $\varepsilon_{hkil} = \left(d_{hkil} / d^0_{hkil}\right) - 1$, where d^0_{hkil} is the "stress-free" lattice spacing. A total of ten stress-free reference coupons ($4 \times 4 \times 4$ mm^3) were machined from the FSP plate (*Case 1*) at 0, ± 5, ± 10, ± 15, ± 20, 120-mm positions using EDM. It was assumed that all macroscopic residual stresses in the coupons were fully relaxed and d^0_{hkil} was measured along the LD, TD, and ND using 2(x) ×

2(y) × 2(z) mm^3 scattering volume. The macroscopic residual stresses were, then, calculated using the three components of the residual strains using Hooke's law:

$$\sigma_{ii}^{hkil} = \frac{E_{hkil}}{1+\nu_{hkil}}\left[\varepsilon_{ii}^{hkil} + \frac{\nu_{hkil}}{1-2\nu_{hkil}}\left(\varepsilon_{xx}^{hkil} + \varepsilon_{yy}^{hkil} + \varepsilon_{zz}^{hkil}\right)\right] \quad (2)$$

where i=*x, y, z* corresponds to LD, TD, and ND, respectively. The elastic constant (E_{hkil}) in any direction of a hexagonal crystal was calculated using the compliance tensors in pure Mg [40]. Note that 45.4 GPa was used for $E_{10\bar{1}1}$ and 0.35 for $\nu_{10\bar{1}1}$ during the SPF analysis. From the Rietveld analysis, the 'average' strains were calculated using $\varepsilon_{ii}^{avg} = \left(2\varepsilon_{ii}^{a} + \varepsilon_{ii}^{c}\right)/3$ (combination of the strains along the a-axis and c-axis) [41] and E (45 GPa), ν (0.35) were used for the 'average' residual-stress calculation.

4. Contour Method

The contour method is a newly-invented method to determine the residual stress over a cross-section [42]. The displacements of the cut surface (surface contour) due to the relaxation of the residual stress from the cutting are compared to the flat original surface contour to analytically compute the residual stresses using an elastic finite element model [43]. Main experimental procedures include: (1) specimen cutting, (2) contour measurement and, (3) data reduction and analysis. A detailed description of the general methodology is published in the literature [27,42-46].

First, the FSP plate (*Case 1*) was cut in half on the same plane where the neutron diffraction measurements were taken. The cut was made using EDM with a 100 μm diameter brass wire with the part submerged in temperature-controlled deionized water. ''Skim cut'' setting was used to minimize cutting induced stresses. A symmetrical clamping arrangement was used to

minimize specimen movement as stresses relaxed. Because the part was distorted, high strength epoxy was used to fill in gaps between the specimen and the clamping plate. The part was cut using a fixed cutting rate of 0.38 mm/minute and took 13.5 hours to complete.

After cutting, the contour of the cut surface in each half was measured using a confocal laser probe scanning with 7-μm diameter spot with ±0.2-μm nominal accuracy [43]. The entire cross-section was mapped using 0.1-mm and 0.34-mm intervals along TD and ND, respectively, Fig. 2(a). The analysis followed published procedure [42]. The contours on the two surfaces were interpolated onto a common grid and then averaged, which removes any errors caused by shear stresses and the inability to measure transverse displacements.

An ABAQUS 6.5. three-dimensional elastic finite element (FE) model was constructed for a half-part after the cut. The sample geometry was meshed with 106,248 bi-quadratic (20 node) reduced integration hexahedral elements, Fig 2(b). The FE model assumed a homogeneous, isotropic, linearly elastic material with E = 45 GPa and ν = 0.35. The signs of the smoothed contour height were reversed to construct the opposite contour and put into the FE model as displacement boundary conditions in the x-direction on the cut surface. The transverse displacements on the cut surface were unconstrained, which enforces the condition that the surface is free on shear stress. After the boundary conditions were enforced in an equilibrium analysis step, the normal stress was extracted from the cut surface. The contour method used in this study only determines the stress component normal to the surface of the cut, i.e., σ_{xx}. However, it is worth nothing that it is possible to determine other stress components with additional work [47,48].

5. Results

5.1. Microstructure and tensile behavior

The microstructure and texture of the as-received base material (AZ31B-O rolled plate) used in this study were reported previously [15]. The average grain size is about 50 μm measured by the linear intercept method. The pole figure shows a strong texture indicating most of the (0002) basal plane normals are parallel to the ND, which is the typical hot-rolling texture of Mg alloys [13-15]. Figure 3(a) shows overall macrostructure of the FSP AZ31B Mg alloy. It shows distinct regions: stir zone (SZ), transition zone (TZ), and heat-affected zone (HAZ). Note that the width of the SZ along the middle is about 8 mm. Figure 3(b) clearly shows the significant decreases of the grain size in the SZ (average 17 μm) compared to the BM. The average grain size in HAZ (87 μm) is, however, larger than that of BM. Furthermore, there is a significant variation in the grain size through the thickness of the plate, Fig. 3(c). A noticeable variation was also found even within a small area (100×300 μm^2) marked in the SZ.

Figure 4 shows the results of the microhardness and chemical composition along the middle in the FSP Mg plate. There were no significant spatial variations in hardness or chemical composition after FSP. The hardness results show some scatter (50~70 H_v), Fig. 4(a), but without any noticeable trends. The similar hardness in the SZ compared to the BM (58~64 H_v) indicates that there is no significant increase in the microhardness after FSP even with the grain refinement observed in Fig. 3(b). It is consistent with recent studies that reported weak influence of the grain size on the hardness changes in FSP AZ31B Mg alloy [6,7]. Figure 4(b) presents the variations of the Mg and Al composition in wt %. It is evident that there is no pronounced variations in the compositions of Mg (95~96 wt %) and Al (3.6~4.0 wt %) compared to those measured in BM (shown as their grey bands).

However, there were significant changes in the tensile behavior after FSP. Figure 5(a) shows tensile stress-strain curves measured using the standard ASTM specimens machined along the LD from the BM and FSP. The BM result shows approximately 110 MPa longitudinal yield strength (σ_{ys}) and a 32 % elongation. The *Case 1* results show significantly different tensile behavior compared to that of BM as well as in between the samples taken at 0 mm and 10 mm from the centerline. Particularly, the 0-mm sample, which is from the SZ, shows a significant reduction in the σ_{ys} (~55 MPa) and an increased elongation (41 %). On the other hand, the *Case 2* shows similar tensile behavior at these two locations, while showing overall reduction in the σ_{ys} compared to the BM. Figure 5(b) shows the ratio of the tensile σ_{ys} between FSP and BM as a function of distance from the centerline. For *Case 1*, at ±30 mm the σ_{ys} is about 70% of the BM, approaching the centerline it increased to over 90%, but right at the centerline it sharply decreases to about 50% of the BM. The significant decrease at 0 mm in the subsize sample is consistent with the result from the standard tensile specimen. In contrast, the tensile results do not show the significant reduction across the centerline in *Case 2*.

5.2. Texture variations after FSP

Figure 6 shows the variations of the reduced peak intensities of the prismatic $(10\bar{1}0)$, basal (0002), and pyramidal $(10\bar{1}1)$ planes along the LD, TD, and ND across the centerline in *Cases 1* and *2*. The fundamental basis and the usefulness of the reduced intensities to describe the spatial variation of the texture in FSP plate, along with the comparison to full pole figures, have been reported previously in the case of an FSP Al alloy [35]. First, the reduced intensity of a particular (*hkil*) reflection provides quantitative insights to the texture variation. Let us consider (0002) in *Case 1*, Fig. 6(b). It shows a reduced intensity of 1.4 for the (0002) peak along the ND

and 0.2 along the TD at the -60 mm position. It indicates that there are approximately 7 times more unit cells with their (0002) plane normal oriented to ND than TD in BM. The relative ratio is comparable to the pole density ratio (previously measured as 7.4) in the (0002) pole figure of the BM reported in ref. 15.

Secondly, the reduced intensities in the SZ of *Case 1* are significantly different compared to the BM or HAZ, Figs. 6(a)-(c). Most notably, Fig. 6(b) shows that the 1.4 reduced intensity along ND at -60 mm increased up to 2.3 at -20 mm and significantly decreased to 0.7 at 0 mm. Furthermore, the TD and ND reduced intensity variations suggest that the basal plane normal is mainly parallel to the ND at BM/HAZ, mostly parallel to the TD near the TZ, and not parallel to either ND or TD in the SZ, Fig. 6(b). On the other hand, the reduced intensity profiles in *Case 2* do not show such significant variations near the SZ, Figs. 6(d)-(f). Although there are visible changes at 8~12 mm of the (0002) reflection, Fig. 6(e), the change was not nearly as significant as *Case 1*, and the prismatic or pyramidal reflections show very little changes. Moreover, the full pole figure measured at 8-12 mm position shows that the texture is similar to the BM (not shown here). Thus, the variation of the reduced intensity (texture) is significant in the SZ in *Case 1*, while almost no variation was observed in *Case 2*. The 'presence' of each reflection in the diffraction profile measured in each orientation is summarized in Table 1 and the implications of 'missing reflections' on the stress analysis will be discussed in Section 6.2.

5.3. Residual stress in the FSP Mg plate

Figure 7 shows the residual stresses measured from the neutron diffraction using both the SPF and Rietveld methods in the FSP Mg plate (*Cases 1* and *2*). Since only the pyramidal $(10\bar{1}1)$ peak exhibited sufficient intensities along all three directions as shown in Table 1, the

longitudinal (σ_{xx}), transverse (σ_{yy}), and normal (σ_{zz}) residual stresses were calculated using the $\left(10\bar{1}1\right)$ data, Fig. 7(a). It shows a peak-and-valley shape that has been seen in FSP Al alloys [22-28]. For example, σ_{xx} shows compressive stress (-40 MPa) at -60 mm, increases to maximum tensile stress (135 MPa) at ±2 mm, and sharply decreases to compressive stress (-10 MPa) around 0 mm. The changes are qualitatively similar for σ_{yy} and σ_{zz}. Figure 7(b) shows the residual stresses obtained using the Rietveld method. The absence of the data points within the ±2 mm is due to the insufficient peak intensity of certain reflections due to the texture distributions in the SZ. Overall, the residual stress determined using the Rietveld method is in good agreement with the SPF results. Figures 7(c)-(d) show the residual stress profiles obtained in *Case 2*. Note that the lattice spacing measured at -60 mm of the plate was used as the "stress-free" lattice spacing. As for *Case 1*, the results for *Case 2* are in good agreement between the two methods. However, contrary to *Case 1*, the results for *Case 2* do not show the sharp decrease in the residual stress near the SZ. More detailed discussion will be presented in Section 6.1.

Figure 8 shows the results from the contour method showing the σ_{xx} measured for the FSP Mg alloy (*Case 1*). The measured displacement contour (about 200 μm variation) was converted to stress following the steps of data analysis described in Section 4. Note that the thickness of the plate is magnified by a factor of 3 for clarity, Fig. 8(a). Significant tensile stresses are observed at ±10 mm and mild compressive stresses further away from the centerline for the required stress balance. Figure 8(b) shows the σ_{xx} profile extracted along the marked three lines and averaged to make it comparable to the sampling volume of the neutron-diffraction measurements. The σ_{xx} profile slows about -30 MPa at ± 150 mm and a maximum of about 90 MPa at -7 mm with a sharp drop to about 20 MPa at the centerline. It is important to note that the significant decrease in the residual stress (~70 MPa) from -7 to 0 mm is consistent with the result of the neutron

diffraction for *Case 1* obtained using the SPF method as shown in Fig. 7(a). For the comparison, the longitudinal residual stress (σ_{xx}) obtained from the neutron diffraction (both SPF and Rietveld) and contour method are plotted in Fig. 9, which show a good agreement.

6. Discussion

6.1. Residual stress in FSP Mg alloy

The influence of the severe plastic deformation during FSP on the texture development and its effect on the longitudinal yield strength (σ_{ys}) will be discussed in this section. Furthermore, the relationship between the σ_{ys} reduction and the reduction of the residual stress will be discussed by contrasting the different experimental observations from *Cases 1* and *2*.

The general trends of the residual stress profiles are similar between *Case 1* (tool pin and shoulder) and *Case 2* (tool shoulder only) in the FSP AZ31B Mg alloy, Fig. 7. This suggests that the dominant source of the residual stress is the frictional heating from the tool shoulder as established for the case of an Al alloy [25]. More interestingly, the results in *Case 1* show a sharp decrease in the residual stress near the SZ unlike *Case 2* (Figs. 7 and 8). For the cases of FSP Al alloys, it was previously reported that the reduction in the residual stress profile observed near the centerline is due to the σ_{ys} reduction from the microstructural softenening (e.g., dissolution and coarsening of strengthening precipitates) caused by the frictional heating mainly from the tool shoulder [24,25,28]. Therefore, the softening effect was observed in both *Cases 1* and *2* of the FSP Al alloy [25,28]. However, in the case of FSP Mg alloy, the softening was observed on in *Case 1*. Furthermore, compared to the residual stress profiles of FSP Al alloys [22-28], the softening near the centerline is quite distinct in the FSP Mg alloy (*Case 1*). It is suggested that the severe plastic deformation from the tool pin, rather than the frictional heating from the tool

shoulder, is causing the texture changes in FSP [35]. The shear plastic flow associated with the severe plastic deformation, which is caused by the tool pin during FSP, creates crystallographic rearrangements of the basal (0002) plane (preferential slip plane) in that the basal planes surround the tool pin surface in the SZ [13-15]. As a result, significant texture changes were clearly observed in the SZ of the FSP Mg alloy (*Case 1*), Figs. 6(a)-(c), while little changes were observed in *Case 2*, Figs. 6(d)-(f). Since the basal plane in the Mg alloy is neither parallel nor perpendicular to the tensile direction (LD) in SZ, the FSP texture near SZ causes the increases in Schmid factor and lower σ_{ys} in SZ compared to BM or HAZ [15]. The effect of severe plastic deformation on the texture variation and, in turn, on the σ_{ys} is clearly manifested in Figs. 5 and 6(a)-(c) for *Case 1*. In contrast, nearly constant σ_{ys} in *Case 2* across the centerline is well-correlated to the fact that there was almost no texture change in *Case 2*, Figs. 5 and 6(d)-(f).

Consequently, the texture-induced σ_{ys} reduction could be the main cause for the residual stress reduction near the SZ observed in *Case 1*. The σ_{ys} profile obtained using the subsize tensile specimens, Fig. 5(b), is qualitatively similar to the residual stress profile, Figs. 7(a) and 8(b). The relationship between the σ_{ys} and residual stress is more evident when comparing the results between *Cases 1* and *2.* The clear decreases in the residual stress of the SZ in *Case 1* cannot be found in *Case 2*, which does not show the σ_{ys} reduction. In summary, the severe plastic deformation caused by the tool pin caused significant texture variation across the centerline in *Case 1*, which resulted in an increase in Schmid factor and reduction in the longitudinal σ_{ys} near the SZ. As a consequence, the residual stress profile of *Case 1* exhibit a sharp decrease in the SZ due to the localized texture-induced softening, which was not observed in *Case 2*.

Finally, the decrease in the σ_{ys} near the SZ in *Case 1* in spite of no corresponding decreases in hardness (Fig. 4a) implies that the microhardness does not represent the macroscopic tensile

properties in the current case where the texture changes is responsible for the softening rather than the dissolution or growth of precipitates in the case of, for example, FSP Al 6061-T6 alloy. In addition, since nearly constant chemical composition was observed in the SZ, HAZ and BM, Fig. 4(b), the presence or dissolution of a new phase or compound to explain the changes in σ_{ys} is not plausible.

6.2. Effect of texture on the residual stress measurements

Neutron-diffraction stress measurement is tricky when the material has a strong texture, large grain size, or inhomogeneous chemical composition [37,39,49]. Mg alloy plate exhibits a strong texture and the SPF results showed insufficient peak intensities from certain specific (*hkil*) planes along certain directions as summarized in Table 1. For example, the (0002) basal plane normal is predominantly oriented to the ND/TD in the BM, Fig. 6(b). Similarly, the missing (0002) diffraction peak within the SZ along TD, Fig. 6(b), which is caused by the strong texture distribution (e.g., basal plane surrounding the pin column) in the FSP Mg alloy, is problematic for the stress analysis. However, since the $\left(10\bar{1}1\right)$ pyramidal diffraction peak was available along LD, TD, and ND, Fig. 6(c), it was used to calculate residual stresses in FSP plate, Fig. 7(a).

The different stress analysis can also provide an erroneous result within the SZ due to the strong texture, Fig. 7(b). For example, the sharp changes in texture across the SZ in the FSP Mg alloy can cause an inhomogeneous distribution of a certain diffraction plane within the scattering volume. This could cause the mismatch between the geometric centroid of the nominally defined neutron gauge volume and the centroid of the actually 'sampled' gauge volume, and results in an artificial shift in the measured d-spacing and errors in the measured strains. Such effect (often called an 'edge effect') is often encountered when the neutron gauge volume is only partially

filled with the specimen during a measurement of stresses near the specimen surface [39,50]. Therefore, the contour method result was essential to eliminate the ambiguities in interpreting the neutron diffraction results due to the texture effect in FSP Mg alloy. Indeed, the contour-method result clearly showed the significant decreases in the macroscopic σ_{xx} within the SZ, Fig. 9. Furthermore, the comparison shows a good agreement within experimental uncertainties. For example, the peak at -7 mm was approximately 90 ±5.0 MPa using the contour method, and 93 ±12 MPa (SPF) and 120 ±26 MPa (Rietveld) using neutron diffraction. Furthermore, the asymmetric distributions of the residual stress between advancing side and retreating side was similarly depicted in both measurements.

7. Conclusions

1. Microstructure, hardness, and chemical composition were examined in a friction-stir processed (FSP) AZ31B magnesium alloy. In spite of the refined grain size no significant variations in the hardness or chemical composition were found in the severely-deformed stir zone (SZ) compared to the heat affected zone (HAZ) and base material (BM).

2. The longitudinal tensile behavior was investigated using the tensile specimens machined along the longitudinal direction from: i) BM, ii) typical FSP plate (*Case 1*, processed using a regular tool with a pin and shoulder), and iii) modified FSP plate (*Case 2*, processed with a tool with shoulder only to minimize plasticity-induced effects caused by the pin). There were significant yield-strength reductions (55% of the BM) in the SZ of *Case 1* while it is not observed in *Case 2.*

3. Spatial texture variation as a function of distance from the FSP centerline was measured using neutron diffraction in *Cases 1* and *2*. The variation of the reduced peak intensity (texture) was analyzed using the prismatic $(10\bar{1}0)$, basal (0002), and pyramidal $(10\bar{1}1)$ reflections and it showed a significant variation in the SZ in *Case 1*, while almost no variation was observed in *Case 2*.

4. Residual stresses were measured using neutron diffraction and contour method. The neutron diffraction results were analyzed using both the single peak fitting (SPF) and Rietveld methods for the FSP Mg plate (*Cases 1* and *2*). For neutron diffraction results, the residual stress profiles show significant decreases near the SZ (± 2 mm) in *Case 1*, while it is not observed in *Case 2*. The contour method result was consistent with the neutron-diffraction results for *Case 1* and it also clearly showed the significant decreases in the residual stress (up to 70 MPa) near the SZ.

5. Overall, similar residual-stress profiles were observed in both *Cases 1* and *2* suggesting that the dominant source of the residual stress is the frictional heating from the tool shoulder. On the other hand, near the SZ, sharp decrease in the residual stress was observed only in *Case 1*, which suggests that it is related to the severe plastic deformation rather than the frictional heat. The severe plastic deformation caused significant texture variation in *Case 1*, which resulted in an increase in Schmid factor and reduction in the longitudinal σ_{ys} near the SZ. As a result, the residual stress profile of *Case 1* exhibit a sharp decrease in the SZ due to the localized texture-induced softening, which was not observed in *Case 2*.

Acknowledgements

This work is supported by the NSF International Materials Institutes (IMI) Program under contract DMR-0231320. This work has benefited from the use of the Los Alamos Neutron Science Center at the Los Alamos National Laboratory, operated by the Los Alamos National Security, LLC for the National Nuclear Security Administration of the U.S. Department of Energy under contract DE-AC52-06NA25396. This research is also sponsored by the Laboratory Directed Research and Development program of Oak Ridge National Laboratory (ORNL), managed by UT-Battelle, LLC for the U. S. Department of Energy under Contract No. DE-AC05-00OR22725. The authors would like to thank S. R. Agnew and D. W. Brown for helpful discussions, and A. Frederick, T. Sisneros, and G. Wang for their help during experiments.

References

[1] Thomas WM, Nicholas ED, Needham JC, Murch MG, Templesmith P, Dawes CJ. International Patent PCT/GB92/02203, GB Patent 9125978.8; 1991, US Patent 5,460,317 1995.

[2] Mahoney MW, Rhodes CG, Flintoff JG, Spurling RA, Bingle WH. Metal Mater Trans A 1998;29A:1955.

[3] Berbon PB, Bingel WH, Mishra RS, Bampton CC, Mahoney MW. Scripta Mater 2001;44:61.

[4] Mishra RS, MA ZY. Mater Sci Eng R 2005;50:1-78.

[5] Esparza JA, Davis WC, Trillo EA, Murr LE. J Mater Sci Lett 2002;21:917-20.

[6] Chang CI, Lee CJ, Huang JC. Scripta Mater 2004;51:509-14.

[7] Wang YN, Chang CI, Lee CJ, Lin HK, Huang JC. Scripta Mater 2006;55:637-40.

[8] Wang X, Wang K. Mater Sci Eng A 2006;431:114-17.

[9] Lee WB, Yeon YM, Jung SB. Mater Sci Tech 2003;19:785-90.

[10] Somasekharan AC, Murr LE. Mater Characterization 2004;52:49-64.

[11] Lim S, Kim S, Lee C, Yim CD, Kim SJ. Metal Mater Trans A 2005;34:1609-12.

[12] Afrin N, Chen DL, Cao X, Janazi M. Mater Sci Eng A 2007, in press

[13] Park SHC, Sato YS, Kokawa H. Metall Mater Trans A 2003;34:987-94.

[14] Park SHC, Sato YS, Kokawa H. Scripta Mater 2003;49:161-66.

[15] Woo W, Choo H, Brown DW, Feng Z, Liaw PK. Scripta Mater 2006;54:1859-64.

[16] Sato YS, Park SHC, Matusunaga A, Honda A, Kokawa H. J Mat Sci 2005;40:637-42.

[17] Lee CJ, Huang JC, Hsieh PJ. Scripta Mater 2006;54:1415-1420.

[18] Morisada. Y, Fujii H, Nagaoka T, Fukusumi M. Mater Sci Eng A 2006;433:50-54.

[19] Santella M, Frederick A, Degen C, Pan TY. JOM 2006;58:56-61.

[20] Feng AH, Ma ZY. Scripta Mater 2007;56:397-400.

[21] ASM International, ASM Speciality Handbook: Magnesium and Magnesium Alloys. Materials Park (OH), 1999.

[22] Sutton MA, Reynolds AP, Wang DQ, Hubbard CR. J Eng Mater Tech 2002;124:215-21.

[23] Staron P, Kocak M, Williams S. Appl Phys A 2002;74:S1161-62.

[24] Peel M, Steuwer A, Preuss M, Withers PJ. Acta Mater 2003;51:4791-4801.

[25] Woo W, Choo H, Brown DW, Feng Z, Liaw PK, David SA, Hubbard CR, Bourke MAM. Appl Phys Letters;2005;86:231902.

[26] Woo W, Choo H, Brown DW, Feng Z, Liaw PK, Mater Sci Eng A 2006;437:64-69.

[27] Prime MB, Gnaupel-Herold T, Baumann JA, Lederich RJ, Bowden DM, Sebring RJ. Acta Mater 2006;54:4013-21.

[28] Woo W, Choo H, Brown DW, Feng Z. Metall Mater Trans A 2007;38:69-76.

[29] Reynolds AP, Tang W, Gnaupel-Herold T, Prask H. Scripta Mater 2003;48:1289-94.

[30] Windsor CG. Pulsed Neutron Scattering, Taylor and Francis:London:1981.

[31] Allen AJ, Hutchings MT, Windsor CG, Andreani C. Adv Physics 1985;34:445-73.

[32] Bourke MAM, Dunand DC, Ustundag E. Appl Phys A 2002;74:S1707-09.

[33] Larsen AC, Von Dreele RB. General Structure Analysis System, GSAS, LAUR 86-748. Los Alamos National Laboratory:2004.

[34] Carr DG, Ripley MI, Holden TM, Brown DW, Vogel SC. Acta Mater 2004;52:4083-91.

[35] Woo W, Choo H, Brown DW, Feng Z. Liaw PK, Vogel SC. Acta Mater 2006;54:3871-82.

[36] Rietveld HM. Acta Cryst 1967;22:151-52.

[37] Holden TM, Suzuki H, Carr DG, Ripley MI, Clausen B. Mater Sci Eng A 2006;437:33-37.

[38] Choo H, Bourke M, Nash P, Daymond M, Shi N. Mater Sci Eng A 1999;264:108-21.

[39] Hutchings MT, Withers PJ, Holden TM, Lorentzen T. Introduction to the Characterization of Residual Stress by Neutron Diffraction, Taylor and Francis:USA:2005.

[40] Kelly A, Groves GW. Crystallography and crystal defects, Longman:London:1970.

[41] Daymond MR, Bourke MAM, Von Dreele RB. J App Phy 1999;85:739-47.

[42] Prime MB. J Eng Mater Technol 2001;123:162-68.

[43] Prime MB, Sebring RJ, Edwards JM, Hughes DJ, Webster PJ. Exp Mech 2004;44:176-84.

[44] Zhang Y, Ganguly S, Edwards L, Fitzpatrick ME. Acta Mater 2004;52:5225-32.

[45] DeWald AT, Rankin JE, Hill MR, Lee MJ, Chen HL. J Eng Mater Technol 2004;126:465-73.

[46] Kartal M, Turski M, Johnson G, Fitzpatrick ME, Gungor S, Withers PJ, Edwards L. Mater Sci Forum 2006;524-525:671-76.

[47] DeWald AT, Hill MR. Experimental Mechanics 2006;46:473-90.

[48] Korsunsky AM, Regino GM, Nowell D. Inter J Solids and Structures 2007;44:4574-91.

[49] Steuwer A, Dumont M, Peel M, Preuss M, Withers PJ. Acta Mater 2007;55:4111-20.

[50] Spooner S, Wang XL, J Appl Cryst 1997;30:449-55.

Table caption

Table. 1. The results of the single peak fitting (SPF) analysis of the diffraction profiles summarizing the presence of the prismatic $\left(10\bar{1}0\right)$, basal $\left(0002\right)$, and pyramidal $\left(10\bar{1}1\right)$ planes along the LD, TD, and ND in both *Cases 1* and *2*. "O" indicates that the reflection is available and "X" denotes that the reflection is missing or of poor quality unsuitable for the analysis due to the texture. The missing reflections are $\left(10\bar{1}0\right)$ peak along ND, $\left(0002\right)$ peak along LD, and $\left(0002\right)$ peak along TD within ±2mm of *Case 1* due to the strong texture in the BM and FSP Mg alloy. Note that only $\left(10\bar{1}1\right)$ peak is available along all three directions allowing the residual-stress calculation.

Table 1

Peak	LD	TD	ND
$(10\bar{1}0)$ **Prismatic**	**O**	**O**	**X**
(0002) **Basal**	**X**	**O***	**O**
$(10\bar{1}1)$ **Pyramidal**	**O**	**O**	**O**

*** Note that the (0002) reflection along TD is missing within ± 2 mm in Case 1**

Figure captions

Fig. 1. Schematic of (a) the friction-stir processing (FSP), (b) tool design, and (c) spatially-resolved neutron-diffraction measurement positions across the centerline of the AZ31B magnesium alloy plate.

Fig. 2. The contour method: (a) surface contour of the cut surface, (b) surface contour constructed by three-dimensional elastic finite element model with hexahedral meshes.

Fig. 3. Optical micrographs of the FSP AZ31B Mg alloy: (a) overall cross-sectional macrostructure, (b) microstructure of the stir zone (SZ), transition zone (TZ), and heat-affected zone (HAZ), (c) microstructure through the thickness of the plate along the centerline. Significant variations of the grain size were observed (i) across the SZ, TZ, and HAZ, (ii) through the thickness, and (iii) even within the SZ (e.g., 100×300 μm^2 region square marked in c).

Fig. 4. (a) Microhardness and (b) chemical composition measured along the middle of the FSP AZ31B Mg alloy. The results show no significant variations as a function of distance from the centerline. The properties measured from the BM are shown as a thin grey band for comparison.

Fig. 5. Tensile test results measured along the longitudinal direction (LD) of AZ31B Mg alloy: (a) tensile stress-strain curves of base material (BM), *Case 1* (at 0 mm and 10 mm), and *Case 2* (at 0 mm and 10 mm); and (b) the ratio of the tensile yield strength (σ_{ys}) between FSP and BM as a function of distance from the centerline. The results from the standard tensile specimens are

shown as the open square for *Case 1* and open circle for *Case 2*. The results from the subsize specimens for *Case 1* are also shown (closed diamond) with a better spatial resolution depicting a clear variation of the longitudinal σ_{ys} across the centerline.

Fig. 6. The reduced intensities of the prismatic $(10\bar{1}0)$, basal (0002), and pyramidal $(10\bar{1}1)$ reflections measured along the middle of the plate thickness across the centerline with their scattering vectors parallel to the longitudinal (LD), transverse (TD), and normal directions (ND): (a) $(10\bar{1}0)$, (b) (0002), and (c) $(10\bar{1}1)$ from *Case 1*; (d) $(10\bar{1}0)$, (e) (0002), and (f) $(10\bar{1}1)$ from *Case 2*.

Fig. 7. Residual stresses in the FSP AZ31B Mg alloy. Longitudinal (σ_{xx}), transverse (σ_{yy}), and normal (σ_{zz}) stresses were measured using neutron diffraction and analyzed using: (a) single peak fitting (SPF) of $(10\bar{1}1)$: *Case 1*, (b) Rietveld refinement: *Case 1*, (c) SPF of $(10\bar{1}1)$: *Case 2*, and (d) Rietveld refinement: *Case 2*. Residual stresses from the Rietveld method within ±2 mm of *Case 1*, Fig. 7(b), are not available due to a strong texture within the SZ.

Fig. 8. Longitudinal residual stress (σ_{xx}) measured using contour method for *Case 1*: (a) cross-sectional contour map of σ_{xx} on y-z plane shown in Fig. 1 and (b) σ_{xx} variation as a function of distance from the centerline. The σ_{xx} profile is the averaged over the three line across the centerline at z = 3.25 and 3.25 ± 1.1 mm following the nodes in the mesh of the finite element modeling.

Fig. 9. Comparison between the longitudinal residual stresses (σ_{xx}) measured using the contour method and neutron diffraction. The diffraction data include single peak fitting (pyramidal peak) and Rietveld results.

FIGURE 1

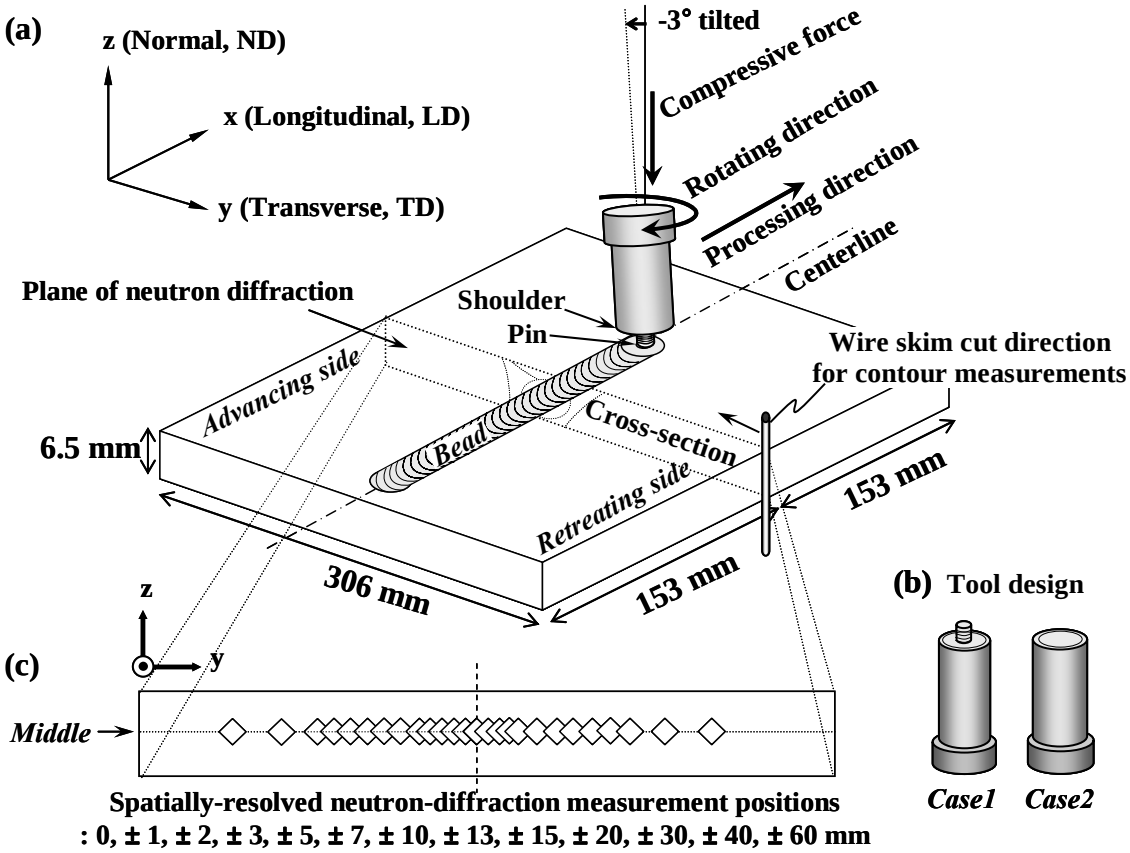
(a)
z (Normal, ND)
x (Longitudinal, LD)
y (Transverse, TD)
-3° tilted
Compressive force
Rotating direction
Processing direction
Centerline
Plane of neutron diffraction
Shoulder
Pin
Wire skim cut direction
for contour measurements
Advancing side
Bead
Cross-section
Retreating side
6.5 mm
306 mm
153 mm
153 mm
(b) Tool design
Case1
Case2
z
y
(c)
Middle
Spatially-resolved neutron-diffraction measurement positions
: 0, ± 1, ± 2, ± 3, ± 5, ± 7, ± 10, ± 13, ± 15, ± 20, ± 30, ± 40, ± 60 mm

FIGURE 2

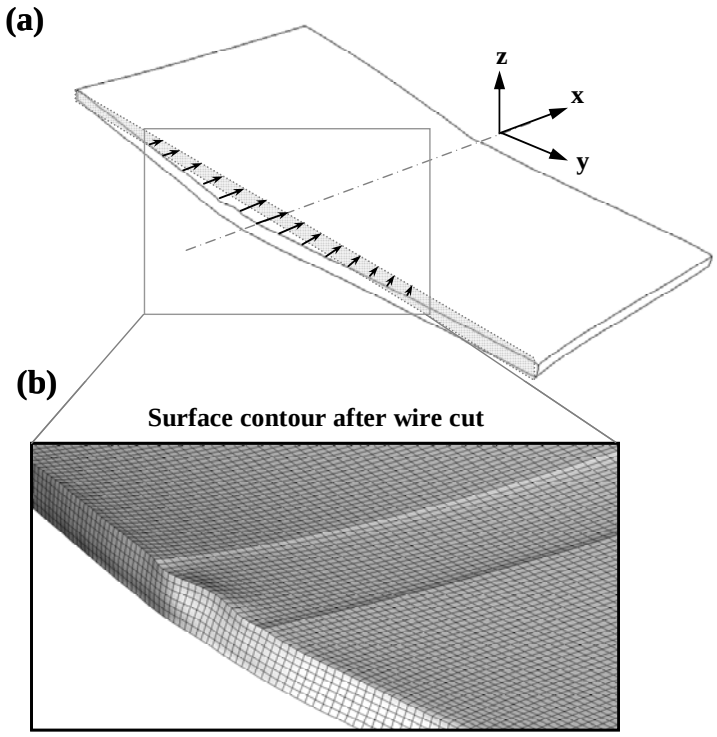

FIGURE 3

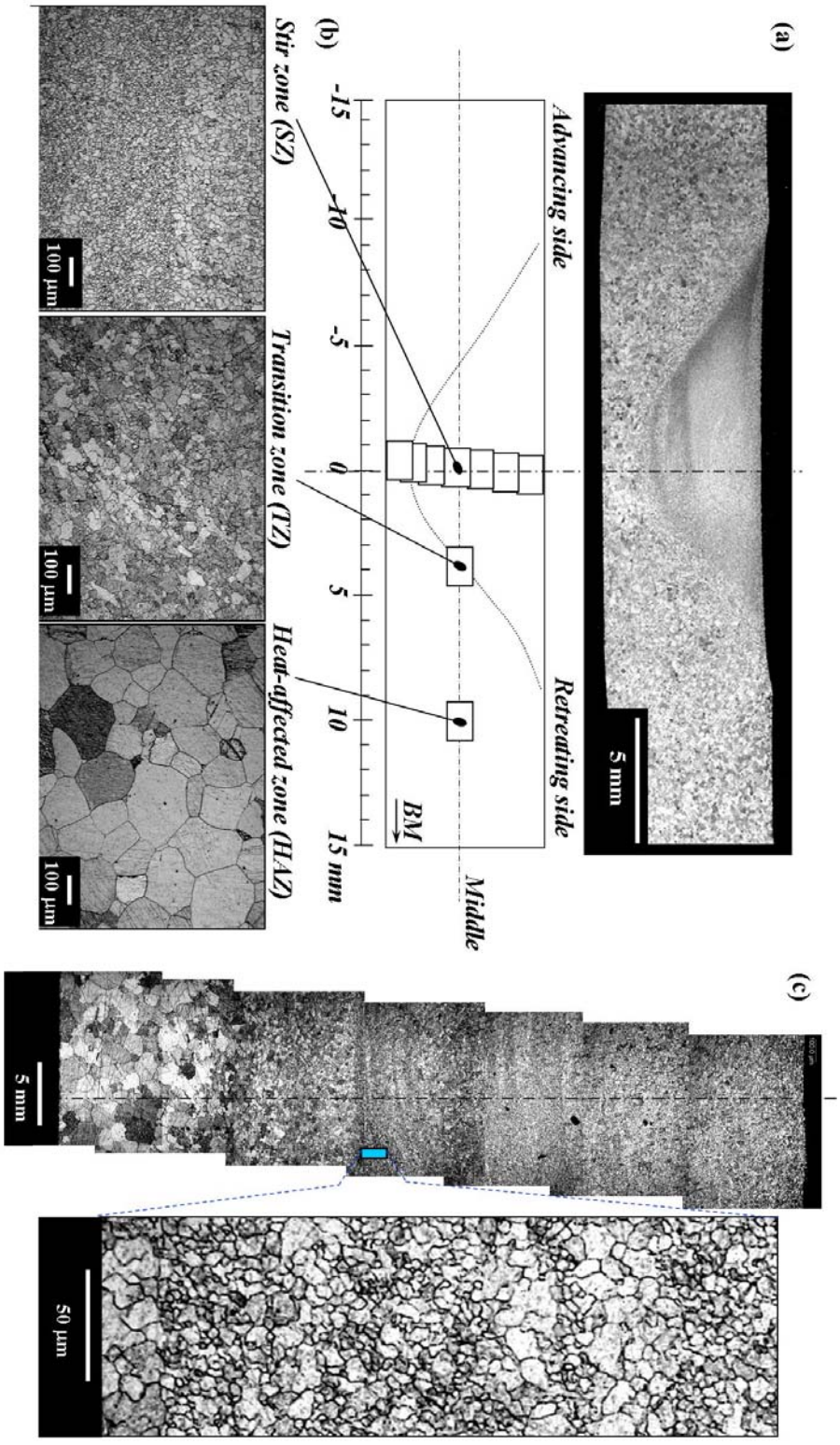
(a)
5 mm
Advancing side
Retreating side
Middle
BM
(b)
-15
-10
-5
0
5
10
15 mm
Stir zone (SZ)
Transition zone (TZ)
Heat-affected zone (HAZ)
100 µm
100 µm
100 µm
(c)
5 mm
50 µm

FIGURE 4

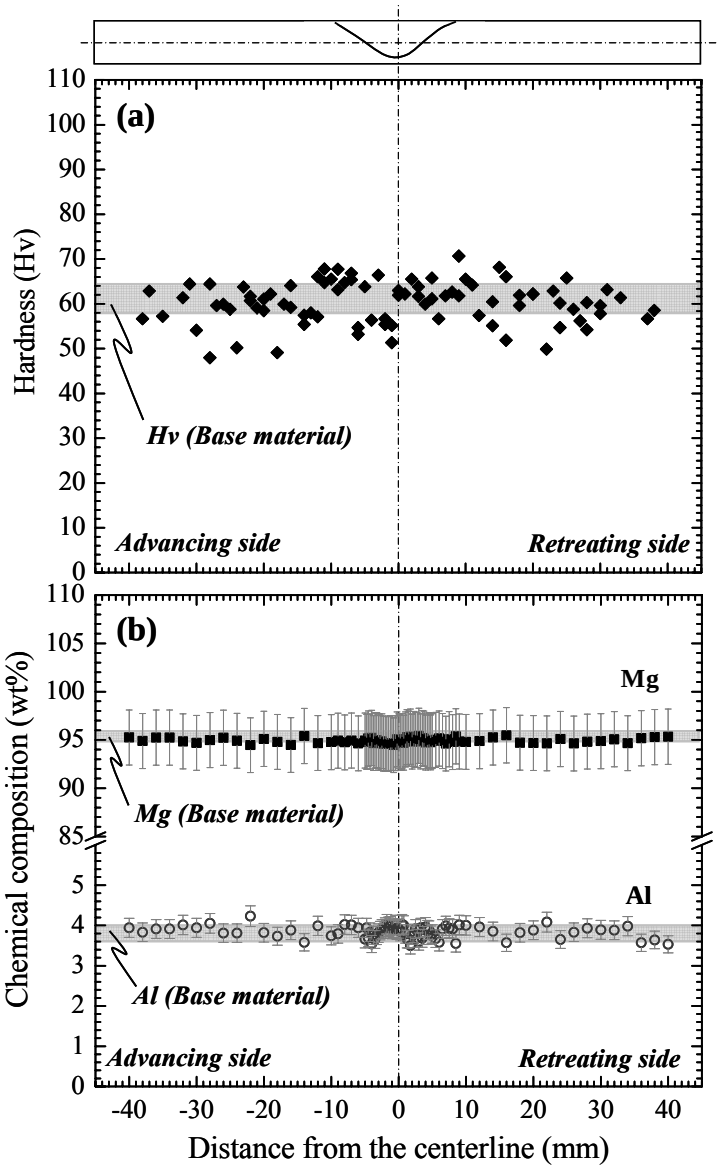
(a)
Hardness (Hv)
Hv (Base material)
Advancing side
Retreating side
(b)
Chemical composition (wt%)
Mg
Mg (Base material)
Al
Al (Base material)
Advancing side
Retreating side
Distance from the centerline (mm)

FIGURE 5

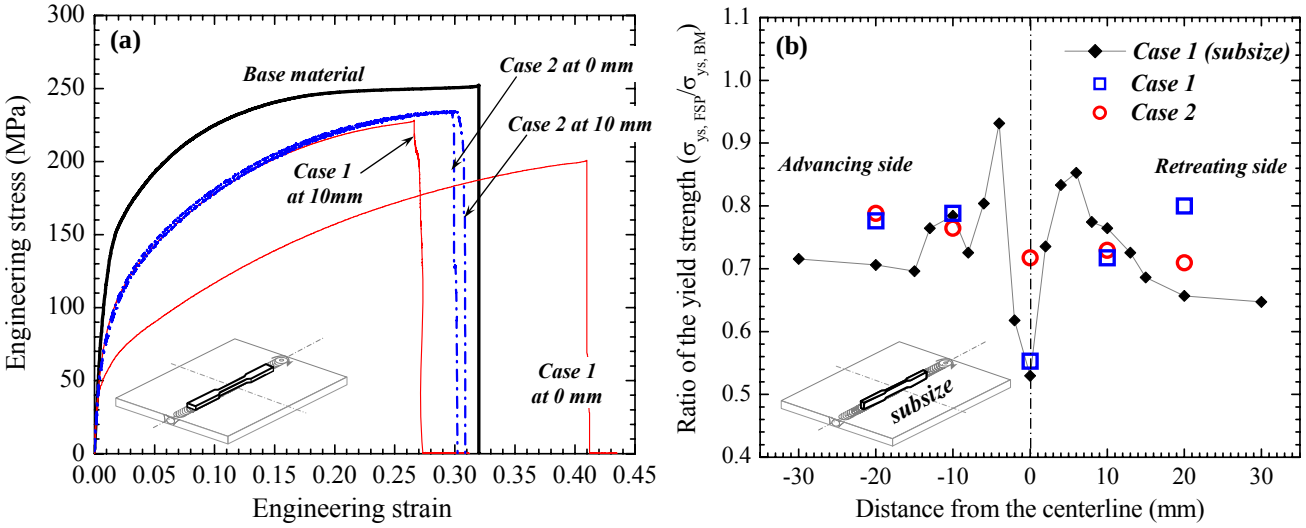
(a)
Base material
Case 2 at 0 mm
Case 2 at 10 mm
Case 1 at 10mm
Case 1 at 0 mm
Engineering stress (MPa)
Engineering strain
(b)
Case 1 (subsize)
Case 1
Case 2
Advancing side
Retreating side
subsize
Ratio of the yield strength ($\sigma_{ys,\,FSP}/\sigma_{ys,\,BM}$)
Distance from the centerline (mm)

FIGURE 6

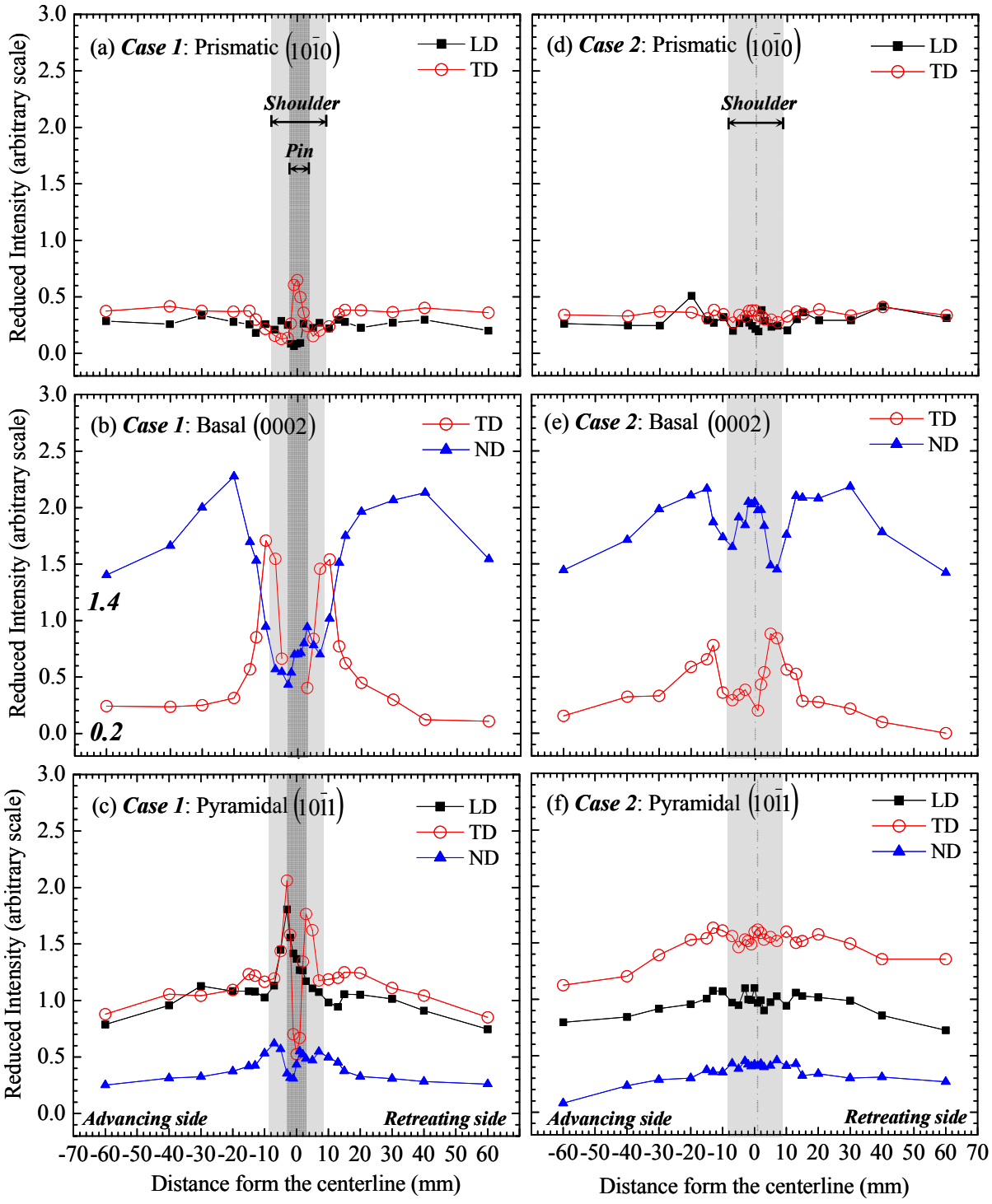
(a) Case 1: Prismatic (10$\bar{1}$0)
LD
TD
Shoulder
Pin
(d) Case 2: Prismatic (10$\bar{1}$0)
LD
TD
Shoulder
(b) Case 1: Basal (0002)
TD
ND
1.4
0.2
(e) Case 2: Basal (0002)
TD
ND
(c) Case 1: Pyramidal (10$\bar{1}$1)
LD
TD
ND
Advancing side
Retreating side
(f) Case 2: Pyramidal (10$\bar{1}$1)
LD
TD
ND
Advancing side
Retreating side
Reduced Intensity (arbitrary scale)
Reduced Intensity (arbitrary scale)
Reduced Intensity (arbitrary scale)
Distance form the centerline (mm)
Distance form the centerline (mm)

FIGURE 7

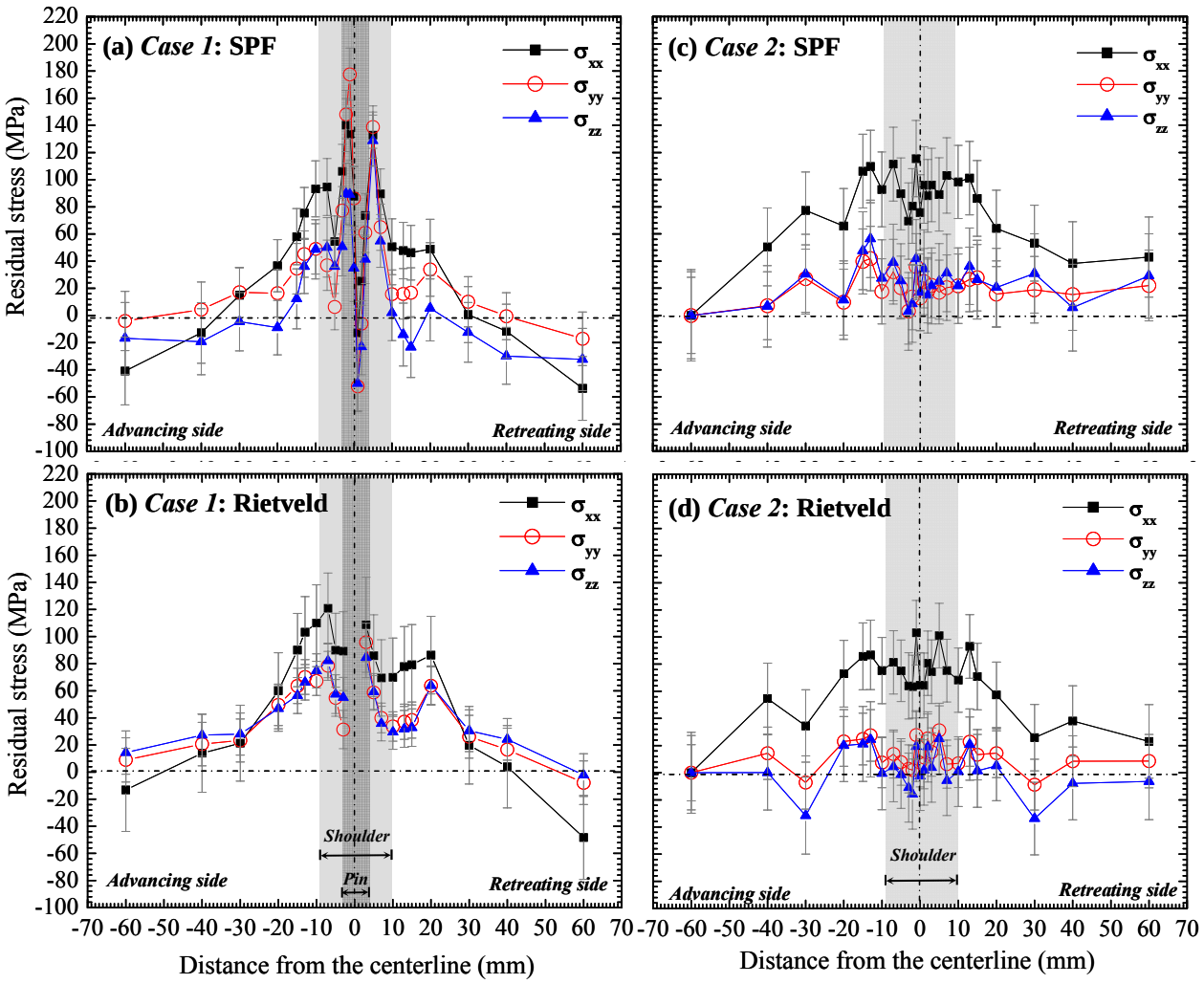
(a) Case 1: SPF
(b) Case 1: Rietveld
(c) Case 2: SPF
(d) Case 2: Rietveld
σxx
σyy
σzz
Residual stress (MPa)
Distance from the centerline (mm)
Advancing side
Retreating side
Shoulder
Pin

FIGURE 8

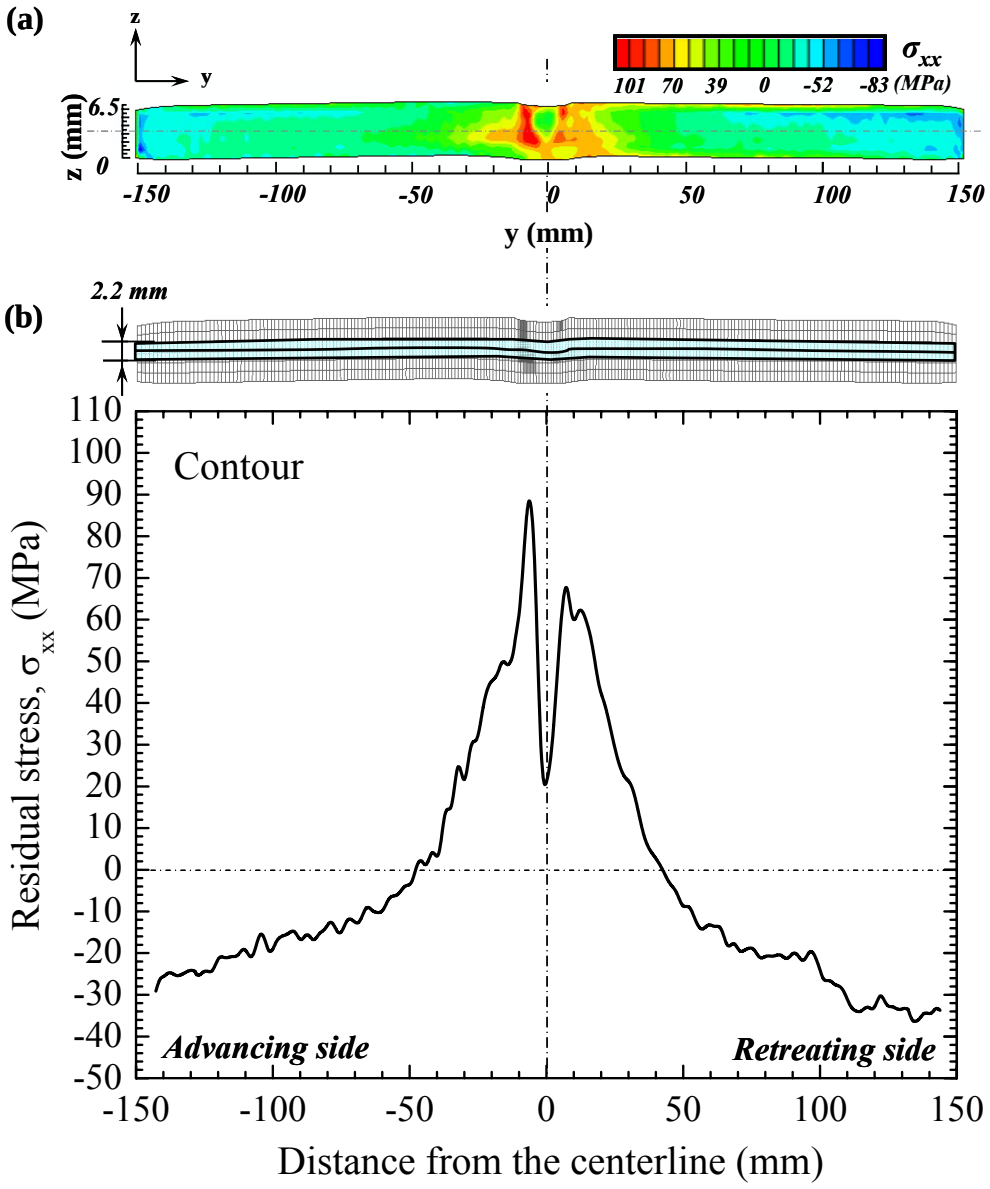
(a)
z
y
σ_{xx}
101 70 39 0 -52 -83 (MPa)
z (mm)
6.5
0
-150 -100 -50 0 50 100 150
y (mm)
(b)
2.2 mm
Contour
Residual stress, σ_{xx} (MPa)
110 100 90 80 70 60 50 40 30 20 10 0 -10 -20 -30 -40 -50
Advancing side
Retreating side
-150 -100 -50 0 50 100 150
Distance from the centerline (mm)

FIGURE 9

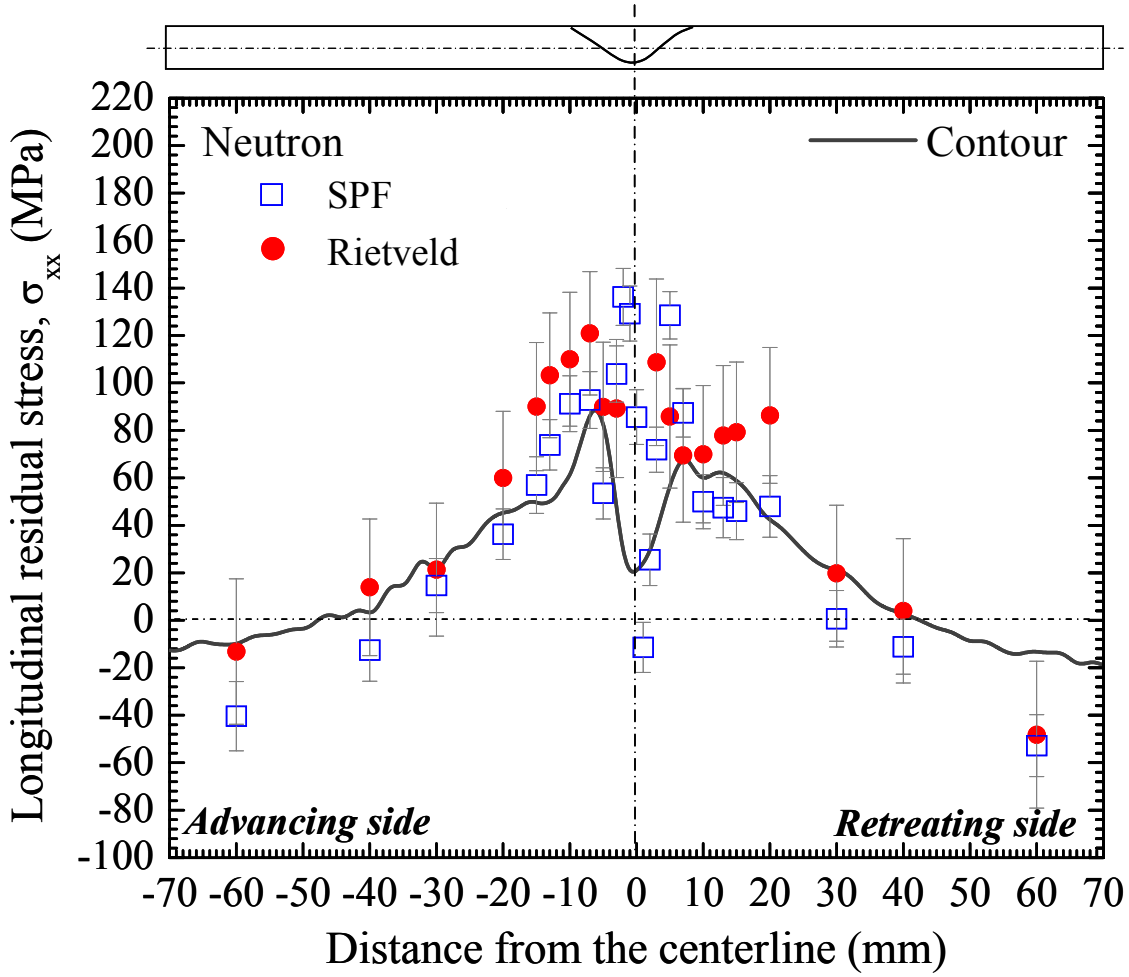
Neutron
SPF
Rietveld
Contour
Advancing side
Retreating side
Longitudinal residual stress, σxx (MPa)
Distance from the centerline (mm)
220
200
180
160
140
120
100
80
60
40
20
0
-20
-40
-60
-80
-100
-70 -60 -50 -40 -30 -20 -10 0 10 20 30 40 50 60 70